Available online at www.sciencedirect.com
ScienceDirect
Journal of Crystal Growth 304 (2007) 374–382
JOURNAL OF CRYSTAL GROWTH
www.elsevier.com/locate/jcrysgro

Synthesis, Raman and X-ray diffraction investigations of rubidium-doped $Gd_{1.8}Ti_2O_{6.7}$ pyrochlore oxide via a sol–gel process

A. Garbout[a,*], S. Bouattour[a], A.M. Botelho do Rego[b], A. Ferraria[b], A.W. Kolsi[a]

[a]*Laboratoire de l'Etat Solide, Faculté des Sciences de Sfax, B.P. 802-3018, Sfax, Tunisie*
[b]*CQFM, IST, Technical University of Lisbon, 1049-001 Lisboa, Portugal*

Received 4 December 2006; received in revised form 26 February 2007; accepted 14 March 2007
Communicated by R. Fornari

Abstract

Nanoparticles of rubidium-doped gadolinium titanates oxide were prepared by the sol–gel process from the titanium alcoxyde $Ti(OBu)_4$ and the two oxides Rb_2CO_3 and Gd_2O_3. Thermal gravimetric (TG) and differential thermal analysis (DTA) results suggest that thermal decomposition of the xerogel takes place when the xerogel is heated at 400 °C. X-ray powder diffraction (XRD) measurements were carried out to study the structure evolution of the sample and to determine the crystalline phases present after heat treatment. A well-crystallized single-phased nanopowder was obtained after calcination at 1000 °C. X-ray diffraction combined to the Raman analysis confirmed the powder's single-phase nature at this temperature. The Rb^+ did not enter the pyrochlore crystal lattice to substitute Gd^{3+} or Ti^{4+} as shown by XRD and X-ray photoelectron spectroscopy (XPS). It is probably dispersed uniformly onto gadolinium titanate nanoparticles. Crystal structure of the non-stoichiometry pyrochlore Rb^+-doped phase $Gd_{1.8}Ti_2O_{6.7}$, was determined using the Rietveld method. Conductivity analysis shows that the presence of Rb^+ dopant in $Gd_{1.8}Ti_2O_{6.7}$ leads to an increase of the ionic conductivity compared to the non-doped $Gd_{1.8}Ti_2O_{6.7}$.

Keywords: A1. Ionic conduction; A1. Thermal analysis; A1. X-ray diffraction; A2. Sol–gel processes; B1. Nanomaterials; B1. Oxide materials

1. Introduction

Sol–gel process has, in the past years, gained much notoriety. It offers new approaches to the synthesis of homogeneous materials with desirable properties of hardness, optical transparency, chemical durability, tailored porosity, and thermal resistance [1]. However, the characteristics and properties of a particular sol–gel inorganic network are related to a number of factors that affect the rate of hydrolysis and condensation reactions, such as pH, temperature and time of reaction, reagent concentrations, catalyst nature and concentration, aging time and temperature, and drying. By controlling these factors, it is possible to vary the structure and properties of the sol–gel-derived inorganic network over wide ranges. In comparison with traditional method, the sol–gel method offers a better chemical homogeneity and low-temperature processing. It allows also the control of the chemical pore size distribution of the nanoparticulate materials [2].

Pyrochlore oxides of general formula $A_2B_2O_7$ exhibit many interesting physical properties such as ferroelectricity and fast ionic conductivity [3]. They are of great interest to a wide community of materials scientists not only because of the fascinating phenomena and properties exhibited, but also due to their potential technological applications in fuel cells and other similar devices. Ideal pyrochlore oxides structure (Fd3m, $Z = 8$), can be considered as an ordered vacancy fluorite structure AX_2 (Fm3m, $Z = 1$) [4]. Compared to the fluorite structure, two kinds of cations are ordered into rows in (1 1 0) directions, resulting in the axes of the pyrochlore unit cell being twice that of the fluorite unit cell. The pyrochlore structure presents two kinds of polyedra, AO_8 and BO_6 and there are two unoccupied O-sites (8(b) site) in the BO_6. Thus, there is a possibility that the oxide ion can be transported via a

---

*Corresponding author. Tel.: +216 23 298 716; fax: +216 74 274 437.
E-mail address: ahlem_garbout1@yahoo.fr (A. Garbout).

0022-0248/$ - see front matter © 2007 Elsevier B.V. All rights reserved.
doi:10.1016/j.jcrysgro.2007.03.021

hopping mechanism through the vacancy sites. This property is improved when the pyrochlores show a non-stoichiometry of the A-site, B-site or O-site [5,6].

The stoichiometric material $Gd_2Ti_2O_7$, which is prepared by traditional solid-state reaction, has been proposed by Raju et al. [7] with a refined unit-cell lattice parameter of 10.185 Å. Preparing sample according to this process generally requires repeated grinding and long heating cycles at temperatures higher than 1200 °C to achieve complete reaction. Yamaguchi et al. [8,9] reported that the doping increases the degree of non-stoichiometry of the $Gd_2Ti_2O_7$ and improved the electrical properties. Recently, Mori et al. [4] confirmed that the standard deviation of the lattice parameters has a tendency to decrease with increasing Gd-site vacancies in the pyrochlore oxide $Gd_2Ti_2O_7$ ($a = 10.1905(4)$ Å).

In this work, we have prepared the rubidium-doped gadolinium titanate compound with the aim to study the impact of the doping rubidium on the structural properties and conductivity. Differential thermal analysis (DTA), thermogravimetric analysis (TG) and X-ray powder diffraction (XRD) were performed to define the conditions of pyrochlore formation. The presence of rubidium in the sample is confirmed by X-ray photoelectron spectroscopy (XPS). The structure of the rubidium-doped pyrochlore was refined. It is quite interesting to compare the conductivity of the rubidium-doped gadolinium titanate to that of other members of this family.

2. Experimental procedure

2.1. Sample preparation

The rubidium-doped gadolinium titanate powder was synthesized by a sol–gel process. This method offers an alternative to produce nanocrystalline materials and chemically homogeneous particles in low crystallization and sintering temperatures. It involves the evolution of inorganic networks through the formation of a colloidal suspension (sol) and gelation of the sol to form a network in a continuous liquid phase (gel) [2]. For the synthesis of crystalline rubidium-doped gadolinium titanate pyrochlore, a series of reaction protocols have been investigated by controlling many factors such as molar ratio, reaction temperature and mutual solvent. The rubidium-doped $Gd_2Ti_2O_7$ pyrochlore with good dispersity was successfully obtained using the following precursors: Rb_2CO_3, Gd_2O_3 and $Ti(OR)_4$ at the molar ratios 0.015, 0.5 and 1, respectively. The synthesis process was as follows: Rb_2CO_3 and Gd_2O_3 were dissolved separately on a solution of acetic acid/octanoic acid (50 vol%) and stirred for 20 min to form transparent solutions, then $Ti(OBu)_4$ was added to the above solution containing Rb_2CO_3 and Gd_2O_3. It was shown that clear monolithic gels rather than colloidal precipitates can be obtained when hydrolysis is performed in the presence of acetic acid. The mixture was then stirred and kept under reflux at 80 °C temperature for 48 h until gelation occurred. The final product was dried at 150 °C for 12 h. The crystal structure and crystallite size of the precipitate depend on the thermal treatment temperature. Both properties are of great importance in the behavior of the material.

The sample was calcinated at different temperatures: 600, 800 and 1000 °C for 3 h.

For the sake of comparison, another sample was synthesized by the same procedure but with only acetic acid and treated at 1000 °C. At this temperature, the powder presented a mixture of $Gd_2Ti_2O_7$ [7] and TiO_2 rutile [10] phases. No structural evolution was shown if the sample was thermally treated at 1400 °C. Fig. 1 shows the X-ray patterns of the two powders synthesized differently and calcinated at 1000 °C.

2.2. Thermal measurements

To determine the thermal character and change of chemical structure of xerogel during calcination process, thermogravimetric analysis (TG) combined with differential thermal analysis (DTA) were performed. A TG–DTA Setaram 92 device was used. Experiments were carried out in air from room temperature up to 600 °C, with a heating rate of 5 °C min^{-1} in a Pt crucible.

2.3. Crystallographic study

XRD was used for identification of crystalline phases by comparison with database by EVA program. The XRD patterns were performed on a D8 Advance Bruker diffractometer, using a Bragg–Brentano geometry, equipped with an energy dispersive detector. Data were collected in the in the range of $10° < 2\theta < 70°$ by step scanning, using 2θ increments of 0.02° and a fixed time of 3 h. An additional powder X-ray diffraction data for the powder calcinated at 1000 °C was collected at ambient temperature in the 12–120° 2θ domain with a 0.02° step and a 25 s per step counting time.

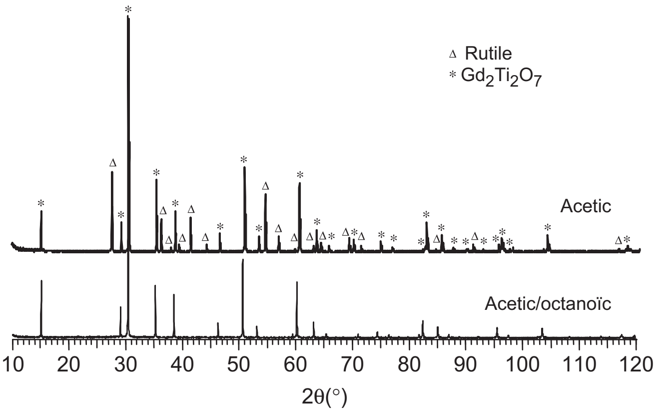

Fig. 1. X-ray diffraction patterns of the obtained powder calcinated 3 h at 1000 °C corresponding to xerogels synthesized with acetic acid and or acetic/octanoïc acids.

Rietveld refinement [11] of the X-ray data was carried out using the FullProf program [12]. The crystallite size can also be determined from the broadening of corresponding X-ray spectral peaks by Scherrer formula [13]: $L = K\lambda/(\beta\cos\theta)$, where L is the crystallite size, λ is the wavelength of the X-ray radiation ($\mathrm{CuK}\alpha = 0.15418\,\mathrm{nm}$), K is usually taken as 0.89, and β is the line-width at half-maximum height. This is the generally accepted method to estimate the mean crystallite size of nanoparticles.

2.4. X-ray photoelectron spectroscopy (XPS)

The XPS spectrometer used was a XSAM800 (KRATOS) operated in the fixed analyzer transmission (FAT) mode, with a pass energy of 20 eV, the non-monochromatized AlKα X-radiation ($h\upsilon = 1486.6\,\mathrm{eV}$) and a power of 120 W ($12\,\mathrm{mA} \times 12\,\mathrm{kV}$). Samples were mounted on a double-face adhesive tape and analyzed under a typical pressure in the range of 10^{-7} Pa. All sample transfers were made in air. Samples were analyzed at room temperature, at take-off angle relative to the surface holder (TOA) of 45°. Spectra were collected and stored in 300 channels with a step of 0.1 eV, and 60 s of acquisition by sweep, using a Sun SPARC Station 4 with Vision software (KRATOS). A Shirley background was subtracted and curve fitting for component peaks was carried out using Gaussian and Lorentzian products. No flood gun was used for neutralizing charge accumulation. As a reference for charge accumulation compensation, contamination C 1s binding energy was set to 285 eV [14]. For quantification purposes, sensitivity factors were 1.80 for Ti 2p, 0.66 for O 1s, 0.25 for C 1s, 1.23 for Rb 3d, and 5 for Gd $3d_{5/2}$.

2.5. Infrared study

The Fourier-transformed infrared (FT-IR) spectra were recorded with an FT-IR spectrometer operated in transmission mode. Prior to analysis, each sample was diluted in IR-grade potassium bromide (5%) by weight and pressed into self-supported discs 8 mm in diameter and approximately 100 mg in weight.

2.6. Raman measurements

The Raman spectra were recorded at room temperature with the 647.1 nm excitation line from a Spectra Physics krypton ion laser. The compound was studied with a very low laser power (3 mW at the sample). Four accumulations of few seconds have been used for each spectral range. No damage of the material by the laser has been observed. The beam was focused onto the samples using the macroscopic configuration of the apparatus. The scattered light was analyzed with a XY Raman Dilor spectrometer equipped with an optical multichannel charge-coupled device liquid nitrogen-cooled detector. In the 15–1000 cm^{-1} frequency range, the spectral resolution is approximately 0.5 cm^{-1}.

2.7. Conductivity measurements

Conductivity investigations were made on sample pelletized at room temperature (diameter 5 mm, thickness ca. 3 mm), then sintered at 1000 °C for 15 h. Gold electrodes were sputtered under vacuum on both flat surfaces of pellets. The sample was placed in a conductivity jig inside a tube furnace. The measurements were obtained by impedance spectrometry in the frequency range 1–10^6 Hz, using a frequency response analyzer Schlumberger 1170; for a given temperature, each set of values was recorded after 1 h stabilization time.

3. Results and discussion

3.1. Thermal analysis

In order to determine the optimum calcination temperature at which the organic template is removed and the inorganic phase is crystallized, themogravimetric analysis (TG) and differential thermal analysis (DTA) measurements were carried out on the xerogel. Fig. 2 shows the TG and DTA curves of the xerogel. The TG curve shows two small weight losses at about 70 and 100 °C accompanied by two endothermic peaks, in the DTA curve, at 72 and 110 °C which are attributed to the elimination of residual water and the dehydration of hydroxide hydrates in the precursors [15,16]. An endothermic peak is to be noticed at 270 °C on the DTA curve, it indicates the melting of the gel [17]. The decomposition and decarbonization of organic species give rise to two exothermic peaks at about 350 and 400 °C in the DTA curve with an important weight loss below 400 °C [18]. These results suggest that the organic template is removed from the xerogel upon calcination at 450 °C.

3.2. X-ray powder diffraction

Fig. 3 displays X-ray powder diffraction patterns of the samples heat-treated in the temperature range 600–1000 °C.

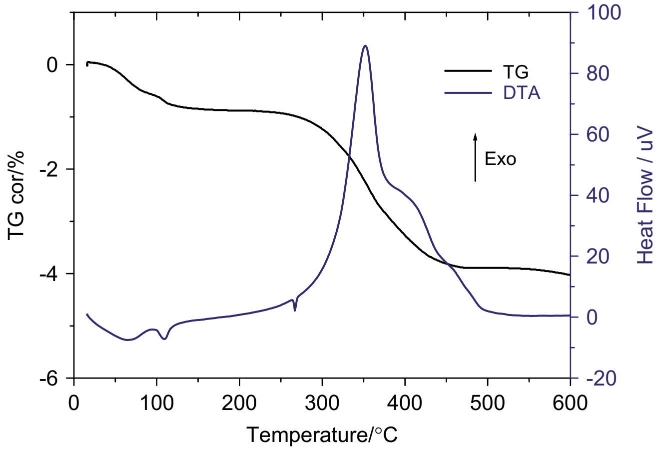

Fig. 2. TG–DTA curves of xerogel synthesized with acetic/octanoïc acids.

At 600 °C, the pyrochlore accompanied with Gd_2TiO_5 [18] start to grow. However, as the calcination temperature increased, the peaks got sharpened likely due to the crystal structure formation. A mixture of $Gd_2Ti_2O_7$ [7] and Gd_2TiO_5 [19] is therefore obtained above 800 °C. At 1000 °C, all diffraction peaks of the sample were indexed as those of the cubic pyrochlore structure. At this temperature, Gd_2TiO_5 phase disappeared completely.

3.3. Structural characterizations

All the reflections in the diffractogram of the sample calcinated at 1000 °C are indexed with respect to the cubic phase of space group Fd3m. However, it was observed that the XRD peaks of $Gd_2Ti_2O_7$ [7] and rubidium-doped $Gd_2Ti_2O_7$ had the same positions by and large suggesting that Rb^+ did not enter $Gd_2Ti_2O_7$ crystal lattice to substitute Ti^{4+} or Gd^{3+}. The relatively huge difference between the Rb^+ (1.49 Å) radius and those corresponding to Ti^{4+} (0.64 Å) and Gd^{3+} (1.19 Å) rationalize that such substitution could not occur and Rb^+ cations are thoroughly dispersed over $Gd_2Ti_2O_7$ particles. Applying the Debye-Scherrer formula and the full-width at half-maximum (FWHM) to the (2 2 2) reflection revealed an average size of about 10 nm for the rubidium-doped $Gd_2Ti_2O_7$ particles.

The Fullprof program [12] was used for the Rietveld refinement. A pseudo-Voigt function was used to describe the profile of Bragg peaks. The starting model of $Gd_2Ti_2O_7$ used in the refinement was based on the crystal determinations report in Ref. [7]. Acceptable Bragg factors and plausible isotropic thermal displacement parameters were obtained, when we assume that there are vacancies in the gadolinium site. With this model, the refinement was stable and converged smoothly. The refinement revealed that a non-stoichiometric compound $Gd_{1.8}Ti_2O_{6.7}$ is obtained. Oxygen vacancies are formed by charge compensation. Similar results are obtained by Mori et al. [20] They confirmed that $Gd_xTi_2O_{7-\delta}$ pyrochlore compounds are synthesized if the Gd content, x, is $1.72<x\leqslant 2.03$.

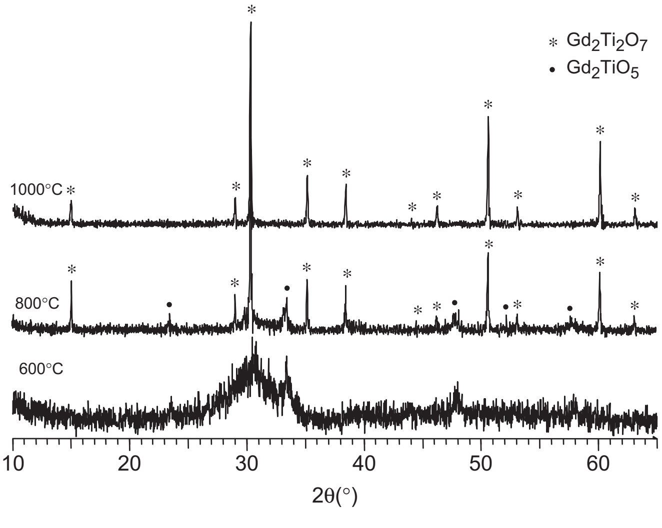

Fig. 3. X-ray powder diffraction patterns of the obtained powder calcinated 3 h at 600, 800 and 1000 °C.

The agreement between the observed and calculated diffraction patterns is shown in Fig. 4. The refinement results are summarized in Tables 1 and 2.

In the rubidium-doped $Gd_{1.8}Ti_2O_{6.7}$ pyrochlore oxide, the Ti^{4+} is located at the center of corner-sharing oxygen octahedra to form the three-dimensional Ti_2O_6 network, surrounding one-dimensional hexagonal channel along the [1 1 1] direction. Although the Gd_2O' chains occupy these holes, they only weakly interact with the more rigid Ti_2O_6 network (Fig. 5). The Ti–O distance (1.983(5) Å) (Fig. 6) is

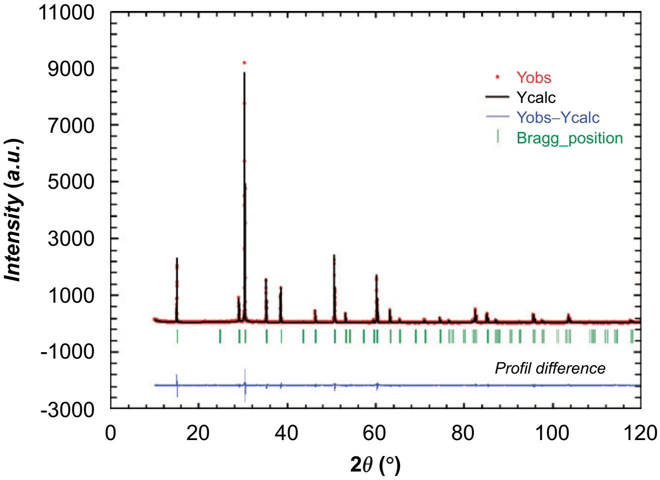

Fig. 4. Rietveld refinement plot showing the observed and calculated diffraction data and their difference for $Gd_{1.8}Ti_2O_{6.7}$.

Table 1
Refinement structural parameters of rubidium-doped $Gd_{1.8}Ti_2O_{6.7}$

Rb-doped $Gd_{1.8}Ti_2O_{6.7}$	
Space group	Fd3m
a (Å)	10.189(3)
V (Å^3)	1057.801(9)
Z	8
χ^2	1.99
R_F	5.78
R_{Bragg}	6.94
R_{exp}	3.83
R_p	5.56

Table 2
Atomic coordinates and occupancy in the unit cell of rubidium-doped $Gd_{1.8}Ti_2O_{6.7}$

Atom	Site	x	y	z	B_{iso}	Occupancy
Gd	16 c	0	0	0	1.153(1)	0.903(2)
Ti	16 d	$\frac{1}{2}$	$\frac{1}{2}$	$\frac{1}{2}$	1.787(7)	1
O	48 f	0.418(1)	$\frac{1}{8}$	$\frac{1}{8}$	1.546 (3)	0.910(4)
O′	8 a	$\frac{1}{8}$	$\frac{1}{8}$	$\frac{1}{8}$	1.301 (3)	1

higher compared to the observed one in $Gd_2Ti_2O_7$ [7] 1.974 Å. The second cation in this structure, Gd^{3+}, is surrounded by eight oxygen atoms in compressed scalenohedral geometry with six long Gd–O and two short Gd–O′ bonds. The Gd–O distance (2.488(4) Å) is lower than the observed one in the pyrochlore $Gd_2Ti_2O_7$ (2.543 Å) [7]. Gd^{3+} cations and O′ anions in this oxide form a three-dimensional network constituted of tetrahedral corner sharing. The Gd–O′ distance, 2.206(2) Å, is similar to the observed one in $Gd_2Ti_2O_7$ [7] (Fig. 7).

Bond lengths for rubidium-doped $Gd_{1.8}Ti_2O_{6.7}$ and $Gd_2Ti_2O_7$ [7] are given in Table 3.

3.4. XPS measurements

Fig. 8a depicts the XPS survey spectrum of the rubidium-doped $Gd_{1.8}Ti_2O_{6.7}$ prepared by sol–gel process after calcination at 1000 °C. The XPS peaks show that the particles contain mainly Ti, Gd, O, Rb and carbon. The C element is ascribed to the residual carbon from precursor solution and the adventitious hydrocarbon from the XPS instrument itself. Its binding energy was, therefore set at 285 eV and used as reference for charge accumulation correction. The binding energies of Ti $2p_{3/2}$, Gd $4d_{5/2}$, O 1s, and Rb $3d_{5/2}$ so obtained were 457.8, 1186.7, 529.5 and 109.6 eV, respectively. All these values are 0.6 to 1 eV lower than the ones found in the literature for the same species—Ti^{4+}, Gd^{3+}, O^{2-} in TiO_2, and Rb^+ [21]. This is a known phenomenon when an external reference is used, especially if an inorganic sample is being analyzed, since an important contact potential may exist between the inorganic sample and the organic contaminant film [22].

The highly symmetric shapes of the titanium XPS lines indicate that the titanium is present only as Ti^{4+}. In fact, the presence of titanium with an oxidation state lower than +4 should have been evidenced by the presence of shoulders on the low binding energy side of the peak, which was not observed [23]. The XPS quantification shows that, at least at the surface, the Ti content is higher than the Gd one. This proves the non-stoichiometry of the gadolinium titanate pyrochlore formed.

The O 1s peaks displayed asymmetric shape with wider left side as shown in Fig. 8b which could be fitted with two components centered at 529.6 and 532.1 eV tentatively assigned to oxide and hydroxyl oxygen chemisorbed on the surface of the sample, respectively [21].

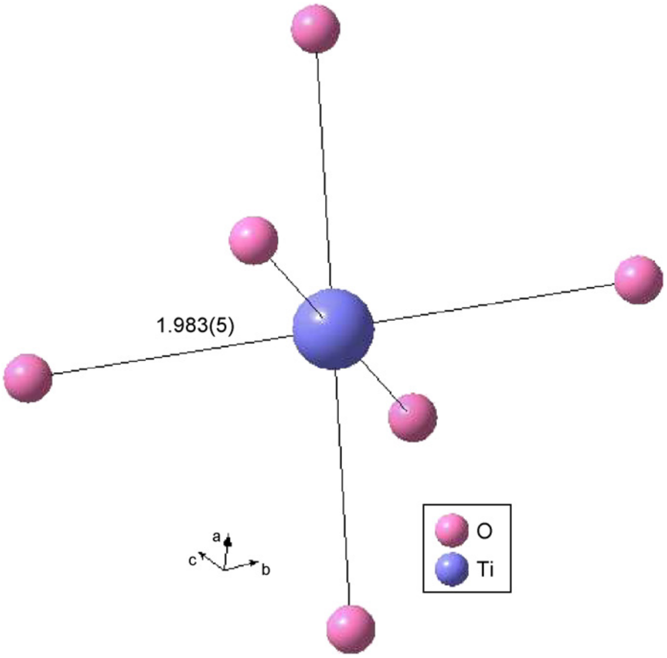

Fig. 6. View of TiO_6 trigonal antiprism in $Gd_{1.8}Ti_2O_{6.7}$ illustrating the coordination around the smaller cation.

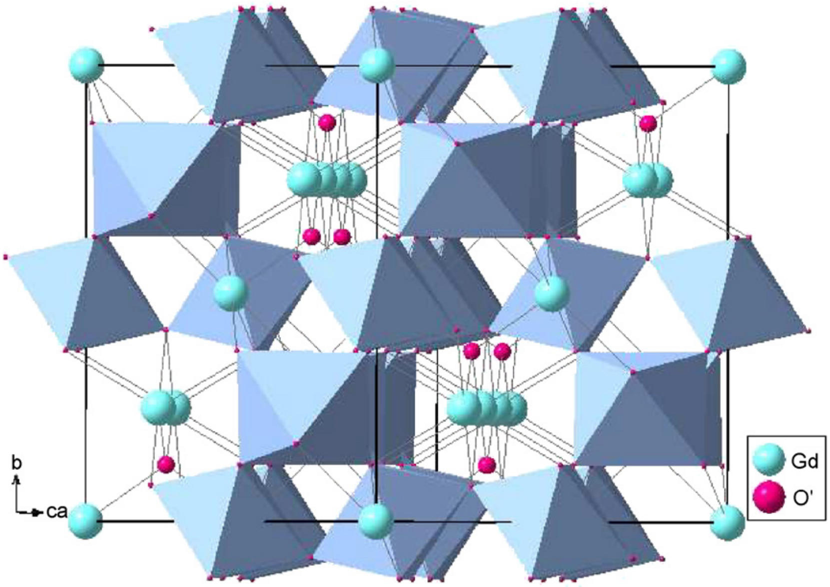

Fig. 5. Cubic pyrochlore structure viewed along the (1 1 0) axis showing Ti octahedra and the Gd cation channels.

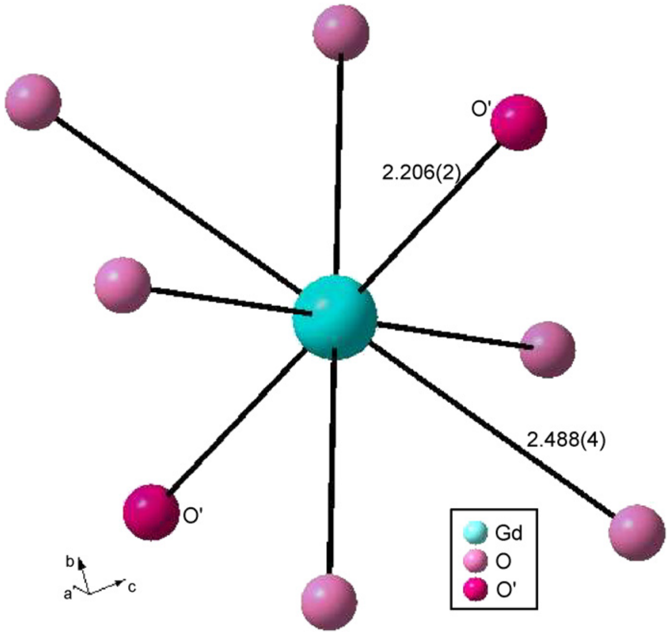

Fig. 7. Gd^{3+} coordination spheres in $Gd_{1.8}Ti_2O_{6.7}$.

Table 3
Interatomic distances (Å) for $Gd_2Ti_2O_7$ and rubidium-doped $Gd_{1.8}Ti_2O_{6.7}$ pyrochlores

$Gd_2Ti_2O_7$ [7]	Rb-doped $Gd_{1.8}Ti_2O_{6.7}$
Gd–O = 2.543	Gd–O = 2.485(5)
Gd–O′ = 2.205	Gd–O′ = 2.206(2)
Ti–O = 1.974	Ti–O = 1.983(5)

The Rb 3d region is composed of a single doublet ($3d_{5/2}$ and $3d_{3/2}$) with a 1.5 eV split denoting the existence of a single rubidium species (Fig. 8c).

3.5. FT-IR spectroscopic investigations

The IR transmittance spectrum of the dried xerogel at 150 °C (Fig. 9) shows a broad band between 3400 and 3700 cm^{-1} which is associated with the fundamental valence vibrations of the hydroxyl groups within the titanols or water. This band is, in general, the result of the following superimposed valence modes: (a) free TiO–H at the surface of the titania gel at 3700 cm^{-1}; (b) hydrogen bonded surface and internal TiO–H at 3550 cm^{-1}; and (c) absorbed water at 3500–3400 cm^{-1} valence band [24]. Fig. 9 exhibits sharp bands around 2900 cm^{-1} corresponding to the stretching vibrations of the aliphatic CH_2 groups [2]. The presence of two bands at 1580 and 1450 cm^{-1} is due to ν_{asym} (COO) and ν_{sym} (COO) [24,25]. The sharp band around 1400 cm^{-1} is characteristic to the bending vibrations of the CH_3 groups [24]. The characteristic bands of δ CO are observed at 1100 and 900 cm^{-1}. The absorption band at 1030 cm^{-1} is associated with the bending of the C–O–Ti linkage [11]. In addition, we observe a peak around 780 cm^{-1} which is attributed to the C=O vibrations. The Ti–O stretching in this sample appears at 570 cm^{-1} [26].

The IR spectra of the investigated rubidium-doped $Gd_{1.8}Ti_2O_7$ pyrochlore calcinated at 1000 °C recorded in the range 400–4000 cm^{-1} is shown in Fig. 9. There are seven IR-active optic modes in the range 750–50 cm^{-1} originating from stretching and bending metal–oxygen bonds in the IR spectra of the pyrochlore oxides with a formula $A_2B_2O_7$ [27]. Subramanian et al. [3] have attributed the band around 600 cm^{-1} (ν_1) to B–O stretching vibrations in the BO_6 octahedron and that around 500 cm^{-1} (ν_2) to the A–O′ stretching vibrations. One broad band at 600 cm^{-1} ascribable to Ti–O stretching vibration was obviously observed. The band at 520 cm^{-1} is just in the region of A–O′ stretching vibration frequency in the tetrahedron of pyrochlore. Hence, it will be reasonable to assign the band to the Gd–O′ stretching vibrations. This is because the stretching vibration frequency (ν) of the bond relates to the reduced mass of the bound atoms [28]. The lower the stretching vibration frequency of the bond, the higher the mass of the bound atoms. The absorption characteristic of νO–H stretching has vanished, due to the water evaporation from the surface of the powder. The sample is deprived of all organic substances contained in the xerogel.

3.6. Raman spectroscopy analysis

Raman spectra of rubidium-doped $Gd_{1.8}Ti_2O_{6.7}$ calcinated at 1000 °C is plotted in Fig. 10. Broad peaks are observed. This is probably related to the small size of nano-rubidium-doped $Gd_{1.8}Ti_2O_{6.7}$ grains in this phase. Similar result is obtained by X-ray diffraction patterns.

The lowest frequency lines, 100 and 210 cm^{-1} are undoubtedly assigned to the F_{2g} mode [29]. The strongest band centered at 310 cm^{-1} is attributed to O–Gd–O bending mode and, in fact, it consists of two modes (E_g, F_{2g}) with very similar frequencies. The band at 450 cm^{-1} was assigned to the Ti–O stretching vibration. Another intense band observed at about 520 cm^{-1} is A_{1g} and attributed to Gd–O stretching [30]. Two very weak bands are also observed at 570 and 690 cm^{-1}. There are no bands assigned to the presence of Gd_2TiO_5. The Raman results confirmed the powder's single-phase nature observed by XRD even when treated at 1000 °C.

It would be more interesting to notice a decrease in the bands frequencies of the rubidium-doped $Gd_{1.8}Ti_2O_{6.7}$ at ca. 100, 210, 520 and 690 cm^{-1} compared to those of $Gd_xTi_2O_{7-\delta}$ [4] and $Gd_2Ti_2O_7$ [31] which is probably due to the effect of rubidium dopant.

3.7. Ionic conductivity

Temperature dependences of the conductivity in the rubidium-doped $Gd_{1.8}Ti_2O_{6.7}$ pyrochlore is studied in the

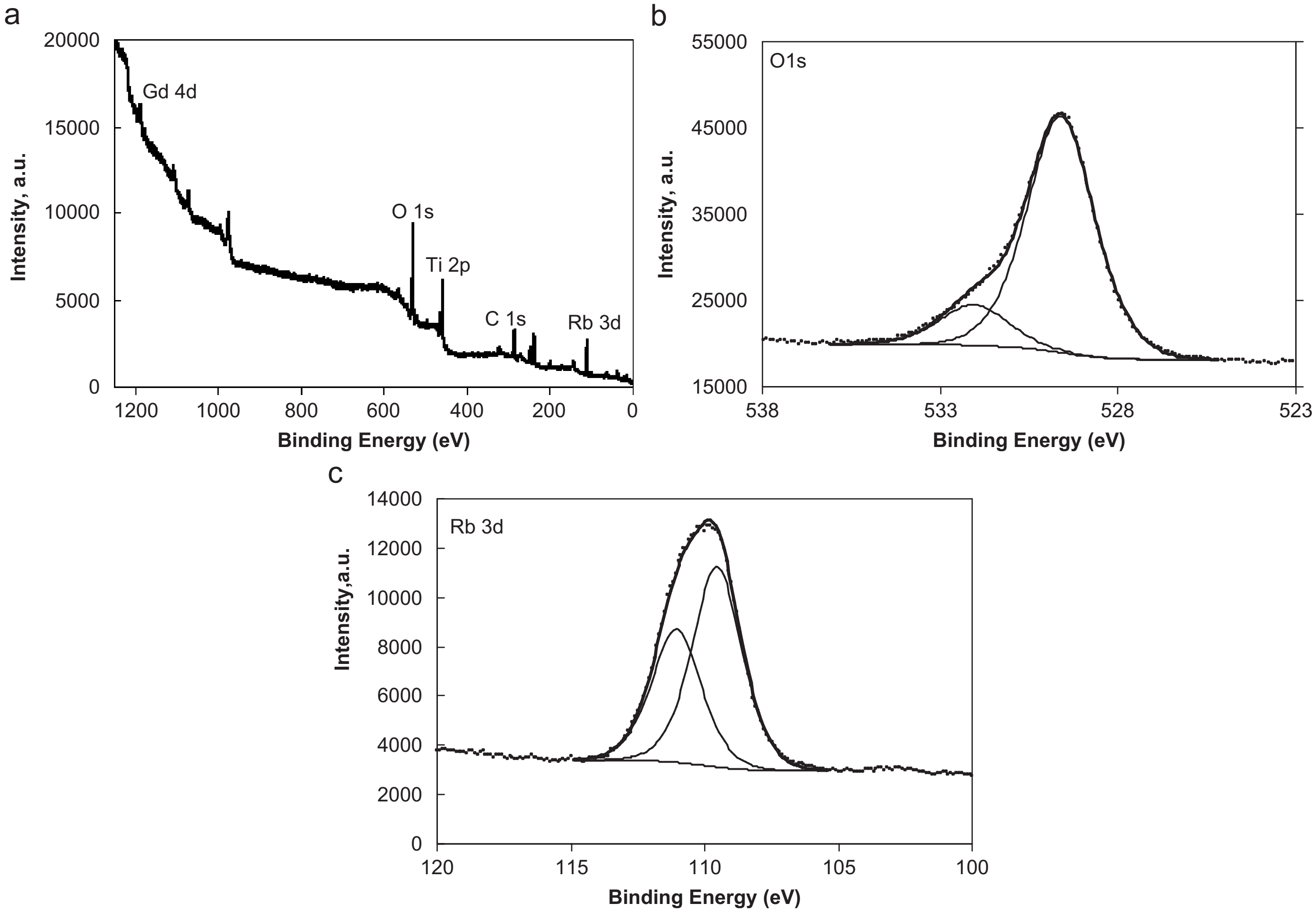

Fig. 8. XPS survey of rubidium-doped $Gd_{1.8}Ti_2O_{6.7}$ pyrochlore calcinated at 1000 °C (a), of O 1s (b) and Rb 3d (c) on the surface of powder prepared using a sol–gel process.

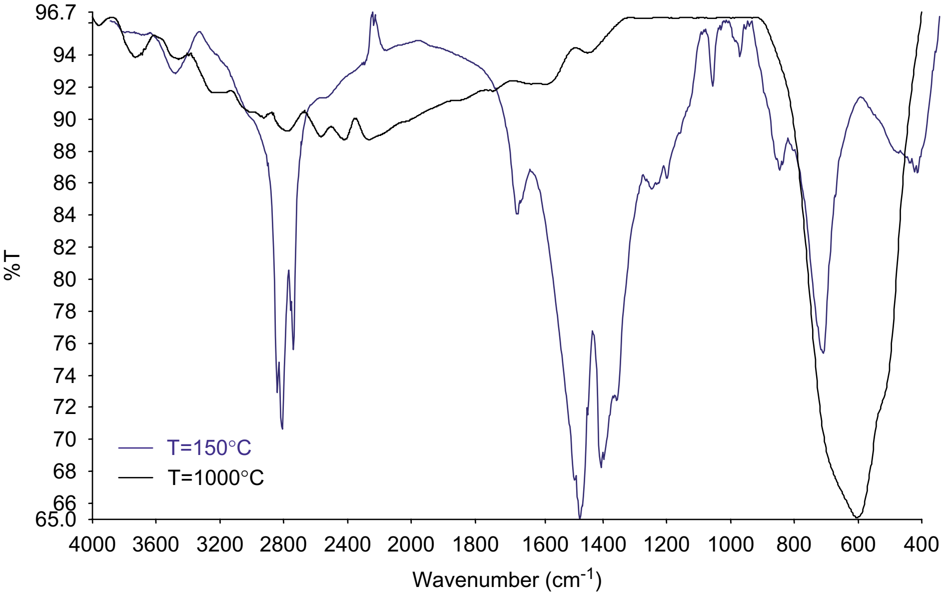

Fig. 9. FT-IR vibration spectrums of the rubidium-doped $Gd_{1.8}Ti_2O_{6.7}$ pyrochlore heated at 150 and 1000 °C.

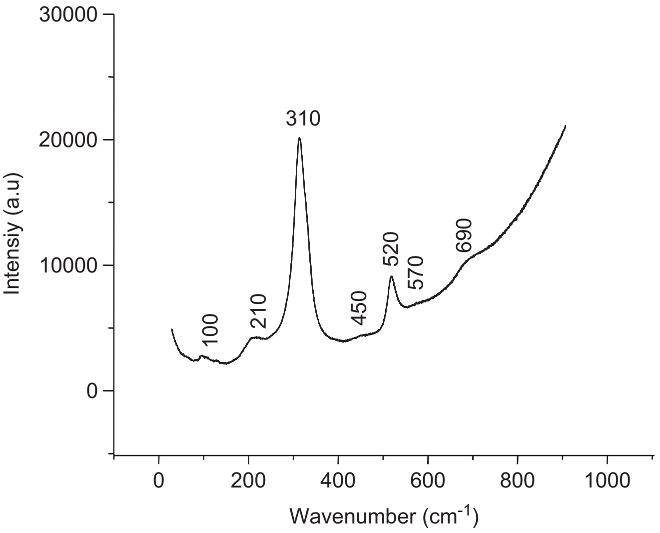

Fig. 10. Raman spectra of rubidium-doped $Gd_{1.8}Ti_2O_{6.7}$ pyrochlore calcinated 3 h at 1000 °C.

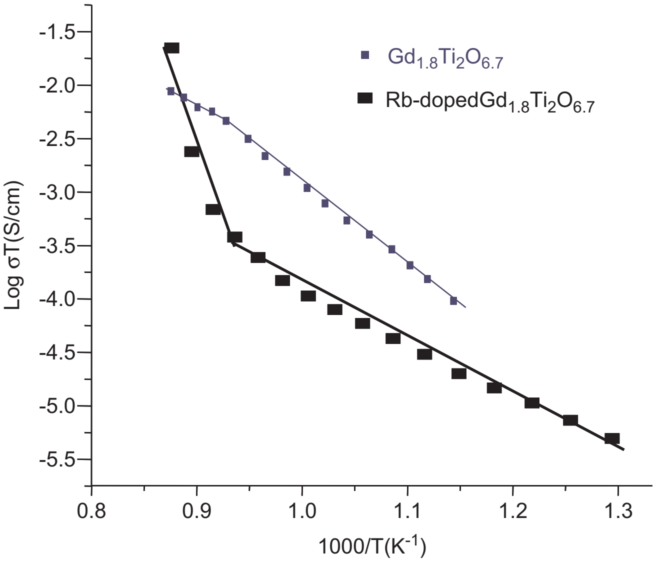

Fig. 11. Relationship of conductivity and temperature for rubidium-doped $Gd_{1.8}Ti_2O_{6.7}$ and $Gd_{1.8}Ti_2O_{6.7}$ pyrochlore during the heating.

temperature range 495–855 °C. In Fig. 11, the Arrhenius plots of the rubidium-doped $Gd_{1.8}Ti_2O_{6.7}$ and $Gd_{1.8}Ti_2O_{6.7}$ are superimposed. From the graph, it is clear that the conductivity of these samples increased with increasing temperature. It should be due to thermally activated hopping conduction of the oxide-ion in this compound. Conductivity should be represented by the function $\sigma T = \exp(-E/k_BT)$, where σ is the conductivity, T is the absolute temperature, E is the activation energy for electrical conduction and k_B is the Boltzmann constant. The activation energy for migration is defined as the difference between the energy of the system when the migrating oxygen ion is at the saddle point and the energy of the oxygen vacancy at equilibrium. It is obtained from the experimental points, fitted by least squares to the equation $\log(\sigma T) = \log\sigma_0 - E/k_BT$. Conductivity plot of Rb-doped $Gd_{1.8}Ti_2O_{6.7}$ shows an onset at 800 °C with a change in activation energy from 0.33 to 1.08 eV, corresponding to the formation of a new high-temperature phase. This lattice value is slightly higher than the observed ones in $Gd_xTi_2O_{7-\sigma}$ (0.93 eV) [4].

The increase in temperature causes probably disordering of the structural vacancies which in turn increases the ionic conductivity [32]. Oxygen ion conduction in this family of compounds proceeds via an oxygen vacancy mechanism [33], which consists of sequential jumps of oxygen ions into vacant sites. The high-temperature phase shows high oxygen conductivity at relatively low temperature. Its value reaches $1.94 \times 10^{-5}\,\mathrm{S\,cm^{-1}}$ at 855 °C, which is higher, compared with the observed one in $Gd_{1.8}Ti_2O_{6.7}$ ($\sigma = 8.76 \times 10^{-6}\,\mathrm{S\,cm^{-1}}$) at the same temperature. The increase of conductivity in the Rb-doped $Gd_{1.8}Ti_2O_7$ can be due to a possible improvement of the surface conductivity and to the quality of the inter-granular contact points.

4. Conclusion

In this paper we report the synthesis method of rubidium-doped gadolinium titanates nanoparticles based on a sol–gel process. DTA and TG results show that decomposition and carbonization of organic substances take place when the xerogel is heated at 400 °C. A well-crystallized single-phased nanopowder was obtained after calcination at 1000 °C. X-ray powder diffraction combined to the Raman analysis confirmed the powder's single-phase nature at this temperature. XRD combined with XPS showed that Rb did not enter pyrochlore crystal lattice to substitute Gd^{3+} or Ti^{4+}. It is probably dispersed uniformly onto gadolinium titanate nanoparticles. The synthesis with the presence of rubidium leads to a non-stoichiometry pyrochlore-doped phase $Gd_{1.8}Ti_2O_{6.7}$. Conductivity analysis shows that the presence of Rb dopant in $Gd_{1.8}Ti_2O_{6.7}$ leads to an increase of the ionic conductivity at 855 °C compared to the non-doped $Gd_{1.8}Ti_2O_{6.7}$.

Acknowledgments

The authors are very grateful to C. Penverne and N. Djelal for X-ray diffraction and TG-DTA characterizations.

References

[1] K.A. Mauritz, JMS-Rev. Macromol. Chem. Phys. C 28 (1) (1988) 65.
[2] S. Doeuff, M. Henry, C. Sanchez, J. Livage, J. Non-Cryst. Solids 89 (1987) 206.
[3] M.A. Subramanian, G. Aravamudan, G.V. SubbaRao, Prog. Solid State Chem. 15 (1983) 55.
[4] M. Mori, G.M. Tompsett, N.M. Sammes, E. Suda, Y. Takeda, Solid State Ionics 158 (2003) 79.

[5] M.P.Y. Jorba, Ann. Chim. t7 (1962) 479.

[6] T. Moriga, S. Emura, A. Yoshihasa, S. Kikkawa, F. Kanamaru, K. Koto, Solid State Ionics 40/41 (1990) 357.

[7] N.P. Raju, M. Dion, M.J.P. Gingras, T.E. Mason, J.E. Greedan, Phys. Rev. B59 (1999) 14489.

[8] S. Yamaguchi, K. Abe, S. Yamazaki, Y. Iguchi, Solid State Ionics 393 (1998) 113.

[9] M.A. Spears, H.L. Tuller, in: T.A. Ramanarayanan, W.L. Worrell, H.L. Tuller (Eds.), Ionic and Mixed Conducting Ceramics Proceedings, vol. 9412, The Electrochemical Society, Pennington, NJ, 1994, p. 94.

[10] I.E. Grey, C. Li, C.M. MacRae, L.A. Bursill, J. Solid State Chem. 127 (1996) 240.

[11] H.M. Rietveld, J. Appl. Crystallogr. 2 (1969) 65.

[12] J. Rodriguez-Carvajal, FULLPROF program for Rietveld refinement and pattern matching analysis, version 3.5d, LLB-JRC, Laboratoire Leon Brillouin (CEA-CNRS), October 1998.

[13] Q.H. Zhang, L. Gao, J.K. Guo, Appl. Catal. B26 (2000) 207.

[14] B.G. Briggs D, High Resolution XPS of Organic Polymers, The Scienta ESCA300 Database, Wiley, NewYork, 1992.

[15] Y. Ohara, K. Koumoto, T. Shimizu, H. Yanagida, J. Mater. Sci. 30 (1995) 263.

[16] D.L. Perry, S.L. Phillips (Eds.), Handbook of Inorganic Compounds, CRC Press, Boca Raton, FL, 1995, p. 216.

[17] G. Xiong, X. Wang, L. Lu, X. Yang, Y. Xu, J. Solid State Chem. 141 (1998) 70.

[18] S. Doeuff, M. Henry, C. Sanchez, Mater. Res. Bull 25 (1990) 1519.

[19] W. Schneider, J. Res. Natl. Bur. Stand., Sect. A 69 (1965) 255.

[20] M. Mori, T. Yamamoto, H. Itoh, T. Watanabe, J. Mater. Sci 32 (9) (1977) 2233.

[21] C.D. Wagner, A.V. Naumkin, A. Kraut-Vass, J.W. Allison, C.J. Powell, J.R. Rumble, NIST X-ray Photoelectron SpectroscopyDatabase, NIST Standard Reference Database 20, version 3.3 (Web Version), 〈http://srdata.nist.gov/xps/〉, 2003.

[22] O. Pellegrino, M. ReiVilar, G. Horowitz, A.M. Botelho do Rego, Mater. Sci. Eng. C22 (2002) 367.

[23] W. Kallel, S. Bouattour, A.W. Kolsi, J. Non-Cryst. Solids 352 (2006) 3970.

[24] K. Nakamoto, Infrared and Raman Spectra of Inorganic and Coordination Compounds, third ed, Wiley, NewYork, 1978.

[25] J. Catterick, P. Thornton, in: H.J. Emeleus, A.G. Sharpe (Eds.), Adv. Inorg. Chem. Radio Chem., vol. 20, Academic Press, New York, London, 1977, p. 291.

[26] M. Picquart, L. Escobar-Alarcon, E. Torres, T. Lopez, E. Haro-Poniatowski, J. Mater. Sci. 37 (2001) 3241.

[27] B.J. Kennedy, Phys. B: Condens. Matter 303 (1998) 241.

[28] H. Du, X. Yao, Mater. Res. Bull. 40 (2005) 1527.

[29] M.T. Vanderborre, E. Husson, J. Solid State Chem. 50 (1983) 362.

[30] M. Oueslati, M. Balkanski, P.K. Moon, H.L. Tuller, Mater. Res. Soc. Sym. Proc. 135 (1989) 199 (Materials Research Society).

[31] N.T. Vanderborre, E. Husson, H. Brusset, Spectrochim. Acta 37A (1981) 113.

[32] M. Pirzada, R.W. Grimes, L. Minervini, J.F. Maguire, K.E. Sickafus, Solid State Ionics 140 (2001) 201.

[33] H.L. Tuller, in: C.R.A. Catlow (Ed.), Defects and Disorder in Crystalline and Amorphous Solids, Kluwer, 1994, p. 189.